Inorganic Chemistry

Article

pubs.acs.org/IC

Structural Features of Sm- and Gd-Doped Ceria Studied by Synchrotron X-ray Diffraction and μ-Raman Spectroscopy

Cristina Artini,*[,†,‡] Marcella Pani,[†,§] Maria Maddalena Carnasciali,[†,∥] Maria Teresa Buscaglia,[‡] Jasper Rikkert Plaisier,[⊥] and Giorgio Andrea Costa[†,§]

[†]DCCI, Department of Chemistry and Industrial Chemistry, University of Genova, Via Dodecaneso 31, 16146 Genova, Italy

[‡]CNR-IENI, Via De Marini 6, 16149 Genova, Italy

[§]CNR-SPIN Genova, Corso Perrone 24, 16152 Genova, Italy

[∥]INSTM, Genova Research Unit, Via Dodecaneso 31, 16146 Genova, Italy

[⊥]Elettra - Sincrotrone Trieste S.C.p.A., ss 14, km 163.5, 34149 Basovizza, Trieste, Italy

Supporting Information

ABSTRACT: A structural study of Sm- and Gd-doped ceria was performed with the aim to clarify some unexplained structural features. $(Ce_{1-x}RE_x)O_{2-x/2}$ samples (RE ≡ Sm, Gd; x = 0, 0.1, ..., 1) were prepared by coprecipitation of mixed oxalates and subsequent thermal treatment at 1473, 1173, or 1073 K in air; they were then analyzed at room temperature both by synchrotron X-ray diffraction and μ-Raman spectroscopy. Two structural models were adopted to fit the experimental data, namely, a fluoritic one, resembling the CeO_2 structure at low RE content, and a hybrid one at higher RE content, intermediate between the CeO_2 and the RE_2O_3 structures. Two main transitions were detected along the compositional range: (a) an RE-dependent transition at the boundary between the fluoritic and the hybrid regions, of a chemical nature; (b) an RE-independent transition within the hybrid region at ~0.5, having a purely geometrical nature. The presence of two finely interlaced F- and C-based structures within the hybrid region was confirmed, and hints of their composition were obtained by μ-Raman spectroscopy. The obtained results indicate a possible explanation for the non-Vegard behavioral trend of the cell parameters.

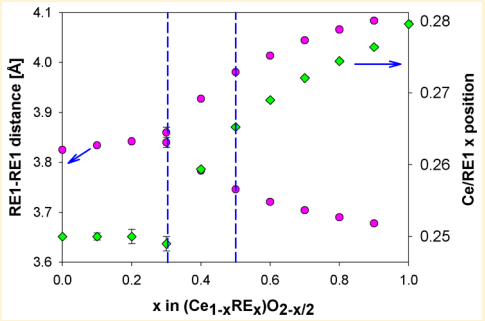

1. INTRODUCTION

RE-doped ceria (RE ≡ trivalent rare earth) forms a family of currently studied oxides to be used as solid electrolytes for solid oxides fuel cells (SOFC's) because of their outstanding conductivity properties:[1] at variance with the commonly utilized Y-stabilized zirconia, where ionic conductivity takes place above 1073 K, CeO_2-based materials can be used in fact at much lower temperatures (673−973 K), allowing significantly decreased operating temperature of the cell.[2,3] In such materials conductivity occurs via oxygen diffusion through the oxygen vacancies introduced by substituting Ce^{4+} with RE^{3+}, and the performance of the electrolyte depends on the RE^{3+} concentration, as well as on the Ce^{4+}/RE^{3+} size mismatch. Gd and Sm result in the best choices among lanthanides in terms of ionic conductivity, and their amount must be limited to a concentration that allows the retention of the CeO_2-based structure, that is, the formation of a CeO_2-based solid solution. In Gd-doped ceria, for example, at 773 K the highest conductivity value is reached close to the composition $Ce_{0.9}Gd_{0.1}O_{1.95}$.[2]

The conductivity performances of these materials are directly related to their crystal structure, but despite the importance of this topic in view of technological applications, many questions related to structural issues are still not completely clear. CeO_2 crystallizes in the fluoritic cubic structure (hereafter named F) belonging to the $Fm\bar{3}m$ space group,[4] which contains four CeO_2 formula units per cell, with lattice parameter a = 5.411 Å.[5] In this highly symmetric atomic arrangement only two atomic positions exist: the (0,0,0) atomic site, occupied by Ce, and the (1/4, 1/4, 1/4) site, occupied by O. Ce is coordinated to eight O atoms building edge-sharing cubes, which are connected to each other to form a three-dimensional chess board. The substitution of Ce^{4+} by a certain amount of a trivalent RE involves the introduction of oxygen vacancies and the formation of a CeO_2-based solid solution up to a certain composition that depends on RE. Beyond this boundary, some additional peaks appear in the diffraction pattern, related to the presence of a superstructure of the fluoritic structure, belonging to the $Ia\bar{3}$ space group, hereafter named C. The C structure is the atomic arrangement typical of sesquioxides of the heaviest rare earths (from Gd to Lu), and it can be considered as formally derived from the fluoritic structure by removing one-fourth O atoms; as a consequence, RE atoms six-coordinate to O, forming corner- and edge-sharing distorted polyhedra. The removal of the O atoms causes a rearrangement of the other

Received: February 18, 2015
Published: April 7, 2015

DOI: 10.1021/acs.inorgchem.5b00395
Inorg. Chem. 2015, 54, 4126−4137

atoms with respect to CeO_2, so that RE atoms are split into two different crystallographic positions. The symmetry reduction causes the doubling of the cell parameter on going from the F to the C structure, and due to the closeness of the ionic sizes of Ce^{4+} and some trivalent rare earths, such as Gd^{3+} and Sm^{3+} (r_{Ce4+} [CN8] = 0.97 Å, r_{Gd3+} [CN8] = 1.053 Å, r_{Sm3+} [CN8] = 1.079 Å, from ref 6), the superposition of the main peaks of both structures, makes the determination of a possible (F + C) coexistence region a nontrivial point.[7] At this stage, it must be pointed out that throughout the paper, ionic sizes of Ce^{4+} and RE^{3+} will be considered with coordination number (CN) 6 or 8, according to the structure they are located in, namely, CN6 for the C and CN8 for the F structure.

In the literature contradictory results can be found regarding the position of the F/C boundary, as well as the exact nature of the C-based structure; differences can arise from the experimental technique employed as well as from the accuracy of the data obtained and the preparation technique of the mixed oxides. According to L. Eyring,[8] RE-doped ceria (RE ≡ Nd, Sm, Gd, Dy, Y, Yb) prepared by solid-state synthesis show a (F + C) biphasic region characterized by an extent that depends on the Ce^{4+}/RE^{3+} size mismatch. Concerning Gd-doped ceria, more recent results generally agree about the existence of a C region beyond the saturation composition of the F-based solid solution, but they are in disagreement about the position of the F/C boundary: the latter has been located either at x = 0.2,[3,9] 0.3,[10] 0.4,[11] or 0.6.[12]

Recently, our research group undertook structural studies of Gd-doped ceria by synchrotron X-ray diffraction (XRD), both at room[13] and at high temperatures,[14] concluding that, for $0 \leq x \leq 0.2$, Gd^{3+} randomly substitutes at Ce^{4+} sites; in this compositional range the creation of oxygen vacancies for the charge compensation occurs without causing significant deformations in the host structure. At higher Gd content, on the contrary, C-based Gd_2O_3 microdomains coherently grow within the F-based matrix. As XRD allows detection of an average situation and does not account for the local structure, a "hybrid" structural model proved helpful to describe the gradual change from the F- to the C-based atomic arrangement with increasing x due to the rising number of Gd_2O_3 microdomains. Studies performed by another research group on Y-,[15] La-,[16] and Gd-doped ceria[17] led to a more complete but analogous scenario: at the local scale (i.e., for r < ~5 Å, with r = interatomic distance range), the system is better described by a biphasic model, consisting in an F-based CeO_2 phase and a C Gd_2O_3-resembling phase; for r > ~10 Å, on the contrary, the biphasic model does not work properly, and the order at the mesoscopic scale fits an average structural model analogous to the one used by us.

In the structural study of the described materials the main shortcoming of XRD is related to the low scattering power of oxygen, which allows to obtain less reliable atomic positions for this element than for rare earths. μ-Raman spectroscopy is a powerful technique able to bypass this inconvenience, thanks to its sensitivity not only to oxygen polarizability but also, and consequently, to oxygen displacement and to any disorder related to the introduction of oxygen vacancies. μ-Raman spectroscopy is particularly useful for the study of RE-doped ceria, as Raman bands belonging to the F-based structure can be easily separated from the ones related to the C-based one, due to the existence of only one active Raman mode in CeO_2, namely, the Ce−O symmetric vibration. Consequently, several studies exist regarding Raman properties of RE-Ce mixed oxides, such as Nd-,[18] Sm[19]-, Lu-, and Sc-doped ceria.[20]

While Gd-doped ceria has been extensively studied, structural issues of Sm-doped ceria have not been fully investigated. Differently from Gd_2O_3, which retains the C structure up to ~1473 K, Sm_2O_3 crystallizes in two different atomic arrangements depending on temperature, namely, in the C structure up to ~1173 K, and in the monoclinic structure (hereafter named B) at higher temperature. In the latter structure, belonging to the $C2/m$ space group, RE assumes two different CN values, namely, 6 and 7, thus forming two different coordination polyhedra. It is then interesting to see whether the crystal structure of Ce−Sm mixed oxides assumes the C-based atomic arrangement, similarly to Ce−Gd mixed oxides, although Sm_2O_3 is not expected to crystallize in the C structure at the temperature considered.

In this work a structural study of Sm-doped ceria, performed at room temperature by synchrotron XRD, is presented. Aim of the study is the determination of the extent of the F-based stability region, as well as the possible existence of Sm_2O_3 microdomains in the CeO_2 matrix at higher Sm content. Making use of the results already obtained for Gd-doped ceria,[13,14] comparisons are made between the two systems, to determine the effect of the RE size in the position of the F/hybrid region (hereafter named H) boundary. Results of XRD are then coupled to μ-Raman spectra collected on samples of both systems prepared at 1473 and 1173 K, with the aim to investigate the mechanism of vacancy formation and the composition of the phases stable in the hybrid region: μ-Raman spectroscopy proved in fact to be a complementary technique to XRD for the evaluation of oxygen displacement and disorder and the determination of the presence of oxygen vacancies. Samples of Sm-doped ceria were prepared at 1473, at 1173, and partly at 1073 K to detect the possible presence of monoclinic Sm_2O_3 at high Sm content and its disappearance with decreasing temperature.

2. EXPERIMENTAL SECTION

2.1. Sample Synthesis. Samples with composition $Ce_{1-x}Sm_xO_{2-x/2}$ (x = 0.1, 0.2, ..., 0.9) were prepared by wet chemistry, to ensure an optimum homogenization. They were obtained by coprecipitation of the corresponding mixed oxalates $(Ce_{1-x}Sm_x)_2[C_2O_4]_3{*}nH_2O$, as described in refs 21 and 22. The synthesis was performed starting from stoichiometric amounts of Ce (Johnson Matthey ALPHA 99.99% wt) and Sm_2O_3 (Alfa Aesar, 99.99% wt), by dissolving them in HCl (13% wt.) and mixing the two solutions. A large excess of an oxalic acid solution was then added to the mixture, causing the immediate precipitation of the mixed oxalates; the precipitates were then filtered, washed with deionized water, and dried in oven at 363 K for 12 h. Mixed oxalates were subsequently thermally treated in air to obtain mixed oxides; two temperatures were chosen, namely, 1173 and 1473 K, with the aim to study the effect of different thermal treatments on the structure of mixed oxides. The issue related to the appearance of monoclinic Sm_2O_3 was further studied by treating oxalates with x = 0.8 and 0.9 also at 1073 K. To compare results obtained from Ce−Sm oxides and from a similar system, Ce−Gd oxides were considered too. $(Ce_{1-x}Gd_x)_2[C_2O_4]_3{*}nH_2O$ samples had been previously prepared by the same coprecipitation method;[13,14] to obtain the corresponding oxides, Ce−Gd oxalates were subsequently treated at 1473 K in air. Commercial CeO_2 (Strem Chemicals, 99.9% wt), Sm_2O_3, and Gd_2O_3 (Alfa Aesar, 99.99% wt.) were treated at 1473 K in air and used as the end members of the sample sets. According to the percent content of trivalent lanthanide and the temperature of the thermal treatment, samples are hereafter named Sm10_1473, Gd10_1473, and so on.

DOI: 10.1021/acs.inorgchem.5b00395
Inorg. Chem. 2015, 54, 4126−4137

2.2. Scanning Electron Microscopy−Energy-Dispersive System. With the aim to check the cationic ratio, all the compositions of Sm-doped ceria were analyzed by means of scanning electron microscopy−energy-dispersive system (SEM-EDS); samples were pressed into pellets, sintered at 1773 K for 1 h, embedded in resin, and polished to the 3 μm grid. Prior to the graphite coating, all the samples were observed by optical microscopy. After polishing, sample with x = 0.9 was thermally etched at 1673 K to highlight the grain morphology and the possible presence of monoclinic Sm_2O_3. Analyses were performed by means of an electronic microscope coupled to energy-dispersive spectrometer Oxford Instruments, model 7353 with Oxford-INCA software v. 4.07, working distance: 15 mm, acceleration voltage: 20 kV. EDS analyses were performed on at least eight points or areas for each sample.

2.3. Synchrotron Data Collection. Ce−Sm oxides prepared at 1073, 1173, and 1473 K, as well as Ce−Gd oxides, were analyzed at room temperature at the powder diffraction beamline (MCX) of the Elettra synchrotron radiation facility located in Trieste, Italy, on a Huber 4-axes X-ray diffractometer equipped with a fast scintillator detector. They were placed in quartz capillary tubes with an inner diameter of 0.5 mm and rotated at a speed of 180 rpm. Diffractograms were collected for $9° \leq 2\theta \leq 60°$ with step 0.01°, counting time 1 s, with the incident beam energy set at 16 keV. Synchrotron data were refined by the Rietveld method by means of the FullProf program.[23]

2.4. μ-Raman. μ-Raman analyses were performed by a Renishaw System 2000 Raman imaging microscope; spectra were collected on powder samples at room temperature as a result of one accumulation, lasting 10 s, by using a 633 nm He−Ne laser in the range of 1000−100 cm^{-1}; they were recorded at least on three points for each sample, with a 50× magnification. The laser power was kept at ∼2 mW; the wavenumber has an accuracy of 3 cm^{-1}.

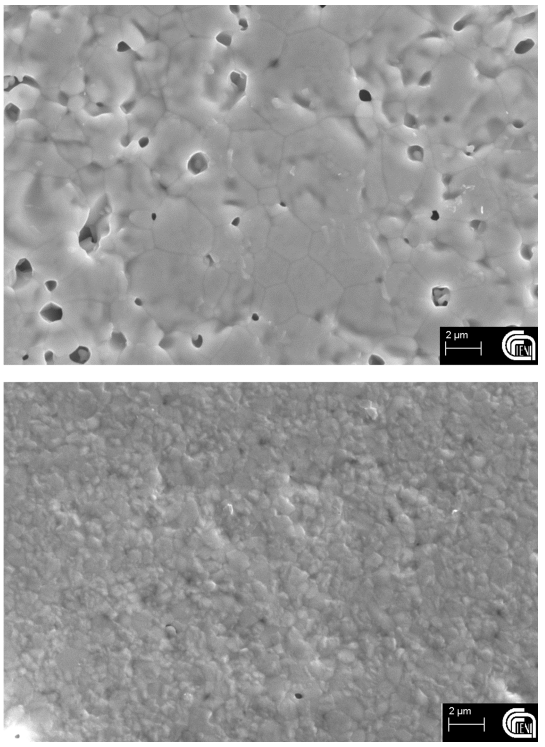

Figure 1. SEM microphotographs taken by secondary electrons on samples (a) Sm10 and (b) Sm90.

3. RESULTS

3.1. Scanning Electron Microscopy−Energy-Dispersive System. SEM microphotographs of all the sintered samples reveal well-connected grains; their sizes span between 2 and 4 μm for all compositions, with the exception of Sm90, which presents smaller grains with an average size of ∼0.5 μm. In Figure 1a,b, images of Sm10 and Sm90 are reported for the sake of comparison. Photos taken by backscattered electrons (not reported) do not show any relevant color variation, thus showing a good homogeneity degree of all the samples and the absence of any secondary phase; this evidence is confirmed by EDS analyses, which do not highlight any noticeable variation among the compositions of different points or areas. The cationic ratio was checked by EDS and was found to correspond to the nominal one within the standard deviation; for this reason the Ce/Sm ratio was fixed to the nominal value in all the Rietveld refinement cycles.

3.2. X-ray Diffraction. Diffraction patterns collected by synchrotron radiation show three different structures, depending on the x value in $Ce_{1-x}Sm_xO_{2-x/2}$ and on the thermal treatment undergone by the samples. For $0 \leq x \leq 0.3$, only peaks corresponding to the fluoritic structure are present in the diffractogram. At x = 0.4, peaks generated by the C superstructure appear, without any peak splitting; the intensity of the superstructure peaks increases with increasing Sm content to x = 0.9. Up to x = 0.8, no significant differences can be appreciated between samples prepared at 1473 and 1173 K. On the contrary, peaks related to B Sm_2O_3 were detected in some Sm-rich samples, namely, in Sm80_1473, Sm90_1473, and Sm90_1173 but not in Sm80_1173.

On the basis of the structures observed, diffraction patterns were refined according to three different structural models, namely, the CeO_2-based F structure, the C-based structure already used for Gd-doped ceria,[13,14] and the B Sm_2O_3 structure. Starting values of cell parameters and atomic positions of the F- and C-based models are reported in the Supporting Information. The C-based model consists of the atomic arrangement typical of the C structure but with atoms located in the ideal positions, that is, as in the F structure. The described model shares properties both with the F and the C structure, but it is not identical to any of them, and it was called for this reason hybrid model. As parameters sensitive to the F → C change (RE1 x coordinate [RE ≡ Ce/Sm], O1 atomic coordinates, O2 x coordinate and occupation factors) are allowed to vary in the refinement cycles, the gradual change from F to C with increasing Sm content can be monitored, as well as the presence of an increasing amount of Sm_2O_3-based microdomains within the fluoritic matrix.

For $0 \leq x \leq 0.3$, refinements were tried both with the CeO_2-based fluoritic structural model and with the hybrid one. For samples with x = 0.1 and 0.2, better agreement factors were obtained by using the fluoritic model, thus confirming the existence of the CeO_2-based solid solution. As Sm enters the structure in the 3+ oxidation state, an oxygen depletion is expected for charge compensation; for this reason, the oxygen occupation factor of the 8c position is allowed to vary during the refinement cycles. For x = 0.3, although the superstructure peaks do not appear, better agreement factors were obtained by using the hybrid model.

For $0.4 \leq x \leq 0.9$, because of the appearance of the superstructure peaks, patterns were refined according to the hybrid model. As mentioned before, patterns of samples with x = 0.8 and 0.9 show the presence of a certain amount of B Sm_2O_3; consequently, Rietveld refinements of such samples included B Sm_2O_3 as a secondary phase. Finally, the pattern of Sm_2O_3 was refined using the monoclinic B structure as a starting model.[24]

DOI: 10.1021/acs.inorgchem.5b00395
Inorg. Chem. 2015, 54, 4126−4137

Table 1. Structural Types, Refined Values of Lattice Parameters, Fractional Atomic Coordinates of RE1, O1, O2, and Occupation Factors of the O2 Site

pattern	structure	cell parameter[a] a [Å]	$x_{Ce/Gd1}$	x_{O1}	y_{O1}	z_{O1}	x_{O2}	sof_{O2}
Sm10_1473	F	10.8444(1)	0.2500(5)					1
Sm20_1473	F	10.8669(2)	0.250(1)					0.936(5)
Sm30_1473	H	10.88937(7)	0.249(1)	0.129(3)	0.382(3)	0.127(6)	0.128(6)	0.93(1)
Sm40_1473	H	10.89875(6)	0.25938(3)	0.1104(6)	0.3704(5)	0.1321(7)	0.1137(8)	0.762(6)
Sm50_1473	H	10.91198(6)	0.26526(7)	0.112(1)	0.362(1)	0.127(1)	0.149(1)	0.72(3)
Sm60_1473	H	10.9151(1)	0.26902(3)	0.1097(5)	0.3609(5)	0.1281(7)	0.1539(9)	0.51(1)
Sm70_1473	H	10.92623(7)	0.27208(2)	0.1061(3)	0.3589(3)	0.1290(4)	0.1525(7)	0.43(3)
Sm80_1473	H + ∼4 wt % B Sm_2O_3	10.92917(8)	0.27444(2)	0.1043(3)	0.3593(3)	0.1274(4)	0.1601(8)	0.363(9)
Sm90_1473	H + ∼29 wt % B Sm_2O_3	10.93076(6)	0.2764(1)	0.103(1)	0.357(1)	0.128(2)	0.160(5)	0.31(3)
Sm10_1173	F	10.8503(1)						1
Sm20_1173	F	10.86570(8)						0.922(5)
Sm30_1173	H	10.8929(1)	0.2495(4)	0.1305(9)	0.387(1)	0.129(1)	0.1392(9)	0.99(1)
Sm40_1173	H	10.90056(5)	0.25895(8)	0.112(1)	0.367(1)	0.139(1)	0.115(2)	0.72(1)
Sm50_1173	H	10.9168(1)	0.26542(9)	0.112(1)	0.361(1)	0.129(2)	0.148(2)	0.62(3)
Sm60_1173	H	10.9195(2)	0.26926(4)	0.1108(7)	0.3588(6)	0.1298(8)	0.153(1)	0.52(1)
Sm70_1173	H	10.92914(8)	0.2718(1)	0.106(2)	0.362(2)	0.130(3)	0.145(2)	0.31(3)
Sm80_1173	H	10.93412(5)	0.27458(3)	0.1055(5)	0.3595(4)	0.1308(5)	0.155(1)	0.28(1)
Sm90_1173	H + ∼15 wt % B Sm_2O_3	10.9324(4)	0.2770(2)	0.099(3)	0.361(3)	0.129(3)	0.15(5)	0.06(2)
Sm80_1073	H	10.92949(6)	0.27408(4)	0.1078(7)	0.3597(6)	0.1310(8)	0.146(1)	0.426(9)
Sm90_1073	H	10.9301(2)	0.2771(2)	0.096(1)	0.363(1)	0.128(2)	0.085(5)	0.243(9)
CeO_2	F	5.4097(1)						1

[a]Cell parameters of patterns refined using the F-structure model were doubled to make them comparable to the other ones.

For each pattern, peak profile matching was done making use of the pseudo-Voigt function, while the background was fitted by linear interpolation of a set of ∼70 points taken from the collected spectrum; when possible, individual thermal parameters B were refined for each Ce/Sm position, and a global B was assigned to both oxygen atoms; nevertheless, in some patterns only the overall thermal parameter was refined, while in other ones it was kept fixed to 0.05, as it assumed a slightly negative value. A synopsis of all the obtained values of thermal parameters, together with the agreement factors, is available as Supporting Information.

In the last refinement cycles, the following parameters were allowed to vary for patterns refined using the hybrid model: the structural parameters (lattice parameter, Ce/Sm1 x coordinate, O1 atomic coordinates, both the x coordinate and the site occupation factor of O2, and the thermal B parameters); the scale factor; five peak parameters; and the background points. The occupancy of O1, initially allowed to vary, was always found slightly higher than 1, and it was then kept fixed to unity. Besides, because of the aforementioned results of EDS analyses, the Ce/Sm cationic ratio was kept fixed to the nominal value. In Table 1 the refined parameters (cell parameter, refinable atomic positions, and O2 occupancy factor) are collected for each sample, except for B Sm_2O_3. In Figure 2 the Rietveld plot of sample Sm60_1473 is reported as an example; all the other Rietveld plots can be found as Supporting Information. The refinement of patterns of the Ce−Gd mixed oxides was performed analogously, as thoroughly described in refs 13 and 14.

As previously described, a certain amount of B Sm_2O_3 appears as a secondary phase in samples with high Sm content (Sm80 and Sm90) prepared at each temperature. As expected from the stability of the different structural forms of rare earth sesquioxides,[4] the B Sm_2O_3 content decreases with decreasing temperature and decreasing Sm content, up to its complete disappearance in samples prepared at 1073 K. Commercial

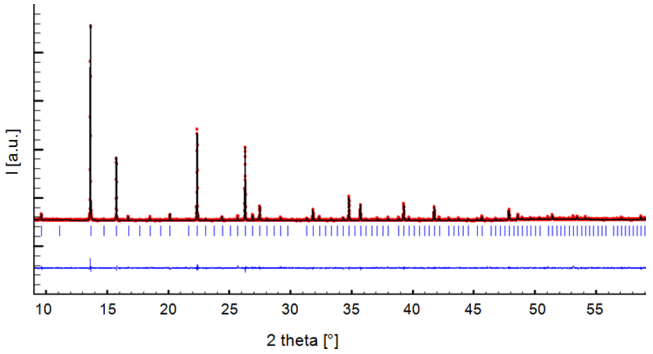

Figure 2. Plot of Rietveld refinement of sample Sm60_1473. The dotted (red) and the continuous (black) lines are the experimental and the calculated diffractograms, respectively; the lower line is the difference curve; the vertical bars indicate the calculated positions of Bragg peaks.

Sm_2O_3, treated at 1473 K, crystallizes in the B structure, as expected from the stability diagram of RE sesquioxides;[4] refined parameters, reported in the Supporting Information together with agreement factors, show a good agreement with literature data.[25]

In Figure 3 the trend of the cell parameters of Ce−Sm and Ce−Gd oxides as a function of RE content is reported. In both cases a nonlinear behavior is observed in the stability region of the hybrid structure; the existence of two distinct phases within the sample can be excluded, as no peak splitting is observed, even by using the high angular resolution provided by the synchrotron radiation. Moreover, the cell parameter values deriving from the CeO_2−Sm_2O_3 mixed system show a linear and increasing behavior from $x = 0$ to $x = 0.3$, that is, in the region where the CeO_2-based solid solution is stable, thus confirming the correctness of the structural model used. In the Ce/Gd system the linear trend in the first compositional range ($0 \leq x \leq 0.2$), not clearly distinguishable due to the low

DOI: 10.1021/acs.inorgchem.5b00395
Inorg. Chem. 2015, 54, 4126−4137

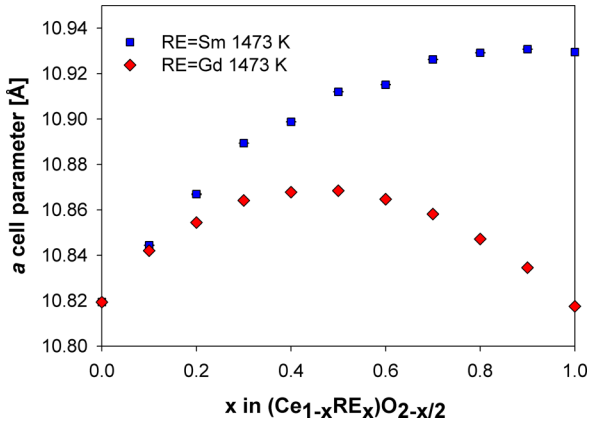

Figure 3. Trend of the cell parameters of Ce−Sm and Ce−Gd oxides as a function of RE content. Error bars are hidden by data markers.

number of experimental points, can be analogously hypothesized after comparison between the two systems.

In Figure 4 the trend of the Ce/RE1 x position as a function of RE amount for both Ce−Sm and Ce−Gd mixed oxides is

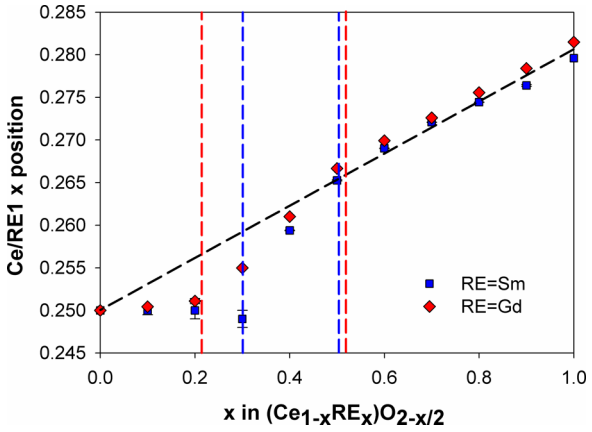

Figure 4. Trend of the Ce/RE1 x position as a function of RE amount for both Ce−Sm and Ce−Gd mixed oxides. Vertical lines indicate the crossing points of the regression lines calculated for the three different regions.

shown; to have refined values of the Ce/RE1 x position to be compared to the other ones, patterns of samples treated at 1473 K with x ranging between 0 and 0.2 were refined also by using the hybrid model. Notice that, in correspondence of the observed appearance of the superstructure peaks (at x = 0.4 for Sm and x = 0.3 for Gd), an abrupt change in the trend of the Ce/RE1 x position appears. While in fact within the existence region of the CeO_2-based solid solution the Ce/RE1 x position assumes a nearly constant value of ~0.25, that is, the value typical of Ce in fluoritic CeO_2, it suddenly moves toward higher values with increasing RE content. By closer inspection, notice that at $x \approx 0.5$ in both systems a slope change is present. Thus, three different behaviors can be observed: (1) for $0 \leq x \leq 0.2$ (in the Ce−Gd system) and $0 \leq x \leq 0.3$ (in the Ce−Sm system), the Ce/RE1 x position assumes a constant value; (2) for $0.2 \leq x \leq 0.5$ (in the Ce−Gd system) and $0.3 \leq x \leq 0.5$ (in the Ce−Sm system), a steep increase is present; (3) for $0.5 \leq x \leq 1$ in both systems a less steep linear behavior can be observed leading to the value typical of the corresponding sesquioxide RE_2O_3. No significant differences can be appreciated by comparing values of Ce−Sm samples treated at 1473 and 1173 K.

The presence of an anomaly at $x \approx 0.5$ is confirmed also by inspecting the trends of bond lengths, as calculated from the refinement results. In Figure 5 the RE1−RE1 distance is

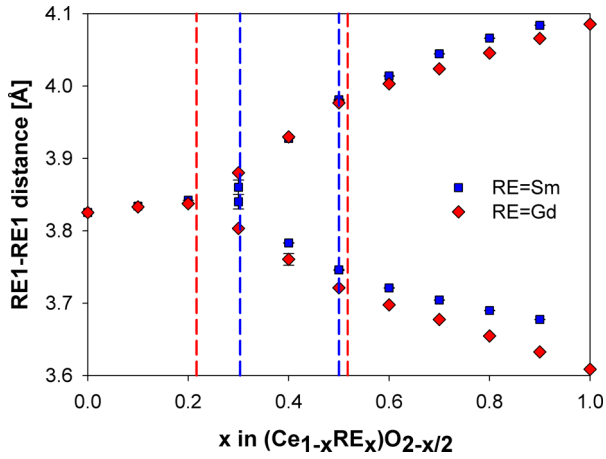

Figure 5. RE1−RE1 bond distance for Ce−Sm and Ce−Gd mixed oxide systems as a function of RE content. Vertical dashed lines indicate the boundary between the different regions in Sm- and Gd-doped ceria.

reported for both systems as a function of the RE amount: up to x = 0.2 or 0.3, depending on RE, a single value is shown, since only one atomic position is available for Ce/RE, and the trend is slightly increasing due to the substitution of Ce^{4+} by the bigger RE^{3+} atom. At higher x, on the contrary, the data set splits into two branches: it can be noticed that a slight slope change appears at $x \approx 0.5$. A similar behavior can be observed also in the RE1−RE2 distance (not shown).

Figure 6 shows the behavior of the O2 occupation factor for both the Ce−Sm and the Ce−Gd systems; as indicated by

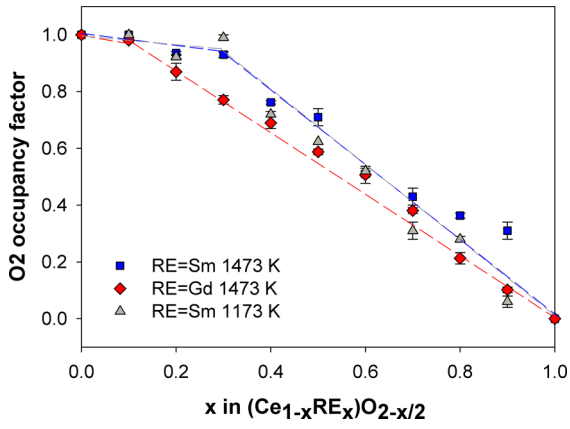

Figure 6. Trend of the O2 occupancy factor for both the Ce−Sm and the Ce−Gd oxide systems as a function of RE content; dashed lines are a guide for the eye.

dashed lines, two trends can be recognized, namely, (1) a nearly constant value from x = 0 to the F/H boundary and (2) a steep linear decrease from the F/H boundary toward 0. A significant deviation from linearity can be observed at x = 0.8 and 0.9 for Sm-containing samples treated at 1473 K, at variance with samples treated at 1173 K.

DOI: 10.1021/acs.inorgchem.5b00395
Inorg. Chem. 2015, 54, 4126−4137

3.3. μ-Raman Spectroscopy. μ-Raman spectra were collected on Sm-doped ceria prepared at both 1473 and 1173 K, as well as on Gd-doped ceria (prepared at 1473 K); peaks of single Raman signals were fitted by interpolating the experimental points with a pseudo-Voigt function; partially overlapping peaks were first deconvoluted and then fitted. The obtained frequencies are reported in the Supporting Information; the accuracy ranges between 0.09 and 1 cm^{-1}, depending on the dopant amount and on the band chosen. In Figure 7 all the spectra collected of Ce−Sm oxides prepared at

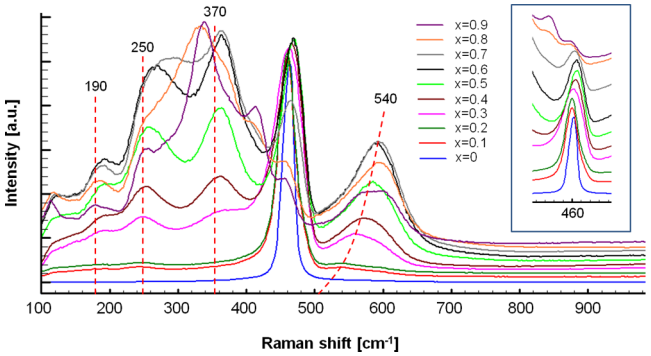

Figure 7. Raman spectra of Sm-doped ceria samples prepared at 1473 K. A shift along the *y* axis was applied to all spectra to separate them. (inset) The spectral region of the main peak is enlarged.

1473 K are shown; for $0 \leq x \leq 0.9$, at a fixed composition, the observed Raman bands are the same for all the series analyzed, slightly differing just for the peak position; only at $x = 1$ spectra are different, showing bands typical of the monoclinic (B) and the cubic (C) structure for Sm_2O_3 and Gd_2O_3, respectively. The only Raman band appearing in the CeO_2 spectrum, located around 465 cm^{-1}, is attributed to the F_{2g} symmetric vibration mode of the Ce−O bond in eightfold coordination.[26,27] Since only oxygen atoms move, the frequency of this signal is expected to be independent of the metal identity: for this reason, effects related to the cation mass are not observed, while any bond length variation or formation of oxygen vacancies will have a direct consequence on the band position and shape. Thus, the cited mode will be used as the most important term for comparison in the following results analysis. Generally speaking, three different behaviors can be recognized through the compositional range from $x = 0.1$ to $x = 0.9$.

(a). $0 \leq x \leq 0.3$ (for Sm-Containing Samples) and $0 \leq x \leq 0.2$ (for Gd-Containing Samples). All spectra are dominated by the signal at ∼465 cm^{-1}, typical of CeO_2, that broadens, decreases in intensity, and becomes progressively more asymmetric with increasing RE amount. At the same time, two additional signals appear at around 540 and 250 cm^{-1}, which become more pronounced with increasing dopant amount. According to Nakajima et al.,[28] these bands are defect-induced Raman signals caused by the introduction of oxygen vacancies into the RE coordination sphere; in particular, they are related to the interaction between the oxygen vacancy and the six next-nearest neighbor oxygen atoms. By closer inspection, it can be noticed that another broad band at ∼600 cm^{-1} is visible. The origin of this defect-induced Raman signal has been differently interpreted, being ascribed either to the introduction of a doping cation into the fluoritic structure forming an REO_8-type complex that does not contain any oxygen vacancy[28] or to the presence of intrinsic oxygen vacancies created by partial reduction of Ce^{4+} to Ce^{3+}.[19,29] Generally speaking, the latter hypothesis is considered as highly probable for nanometric samples treated at 1300−1400 °C, where both the surface-to-volume ratio and the treatment temperature are high enough to enable a non-negligible oxygen loss.[30,31] The Raman spectrum of our CeO_2 sample, on the contrary, does not show any hump close to 600 cm^{-1}; this evidence allows us to conclude that also Gd- and Sm-doped samples do not present any appreciable intrinsic oxygen depletion and that the signal at ∼600 cm^{-1} has an extrinsic nature; that is, it is caused by the presence of vacancies created by the introduction of a trivalent doping ion. The signature of C RE_2O_3 appears at $x = 0.3$ and 0.2 for Sm- and Gd-doped samples, respectively, as a further very broad signal at ∼370 cm^{-1}, which sharpens with increasing x; it is assigned to an (A_g + F_g) RE-O symmetrical stretching mode with RE in six-fold coordination.[32] The appearance of this band at a composition that, according to XRD data, should be characterized only by the fluoritic structure, is not surprising, and it has been already observed for other systems, such as Er-[33] and Tm-doped ceria.[34] This phenomenon is due to the high sensitivity of Raman spectroscopy toward oxygen displacement and to the lower coherence length, with respect to XRD, necessary to detect the existence of microdomains of minor phases.

(b). $0.4 \leq x \leq 0.6$ (for Sm-Containing Samples) and $0.3 \leq x \leq 0.6$ (for Gd-Containing Samples). Five sharp Raman bands are visible, indicating the contemporary presence of a fluorite-related phase and of C $(RE,Ce)_2O_3$. The band at ∼465 cm^{-1} progressively decreases in intensity, while the signal at ∼370 cm^{-1}, and the two bands related to the presence of oxygen vacancies at 540 and 250 cm^{-1}, increase. Starting from $x = 0.4$, it is also possible to detect the presence of a further band at ∼190 cm^{-1}, attributed to the interaction between the oxygen vacancy and the four nearest neighbor metal atoms.[28] Again from $x = 0.4$, the band at ∼600 cm^{-1}, observable in samples at lower RE content, is concealed by the more intense signal at ∼540 cm^{-1}; the disappearance of the cited band indicates that with increasing x the effect of the increased amount of oxygen vacancies tends to prevail over the REO_8-type complexes, as suggested in ref 28.

(c). $0.7 \leq x \leq 0.9$. At $x = 0.7$ the signal related to the presence of the C phase starts to prevail over the one of the fluoritic phase; at the same time all the bands due to the fluoritic phase and to the oxygen vacancies (i.e., at ∼465, 540, 250, and 190 cm^{-1}) decrease in intensity, until they become hardly visible at $x = 0.9$. B RE_2O_3 is detected at $x = 0.8$ and 0.9 at all the temperatures considered both for Sm- and Gd-containing samples, due to the presence of the band at ∼414 cm^{-1}. Other signals typical of B RE_2O_3, namely, the ones at ∼247, 460, 180, and 570 cm^{-1}, are visible only in Sm-doped ceria at $x = 0.9$ at 1473 K; due to their position, they partly hinder the identification of some bands deriving from the F phase, the latter being very weak at such low Ce amount. As expected from the results of XRD, the intensity of the B RE_2O_3 bands increases with increasing temperature and x; the presence of B Gd_2O_3 in Gd-doped ceria, not detected by means of XRD, is on the contrary revealed by the Raman technique due to its high sensitivity to the oxygen displacement.

Finally, the Sm_2O_3 spectrum presents only signals related to the monoclinic form of the sesquioxide, while Gd_2O_3 shows the bands typical of the cubic C structure.

By closer inspection, notice that the peak positions associated with each of the cited Raman modes show a different trend as a

DOI: 10.1021/acs.inorgchem.5b00395
Inorg. Chem. 2015, 54, 4126−4137

function of x. In Figure 8a the Raman frequencies of the band located at ∼465 cm^{-1} are shown for Sm-doped ceria: three

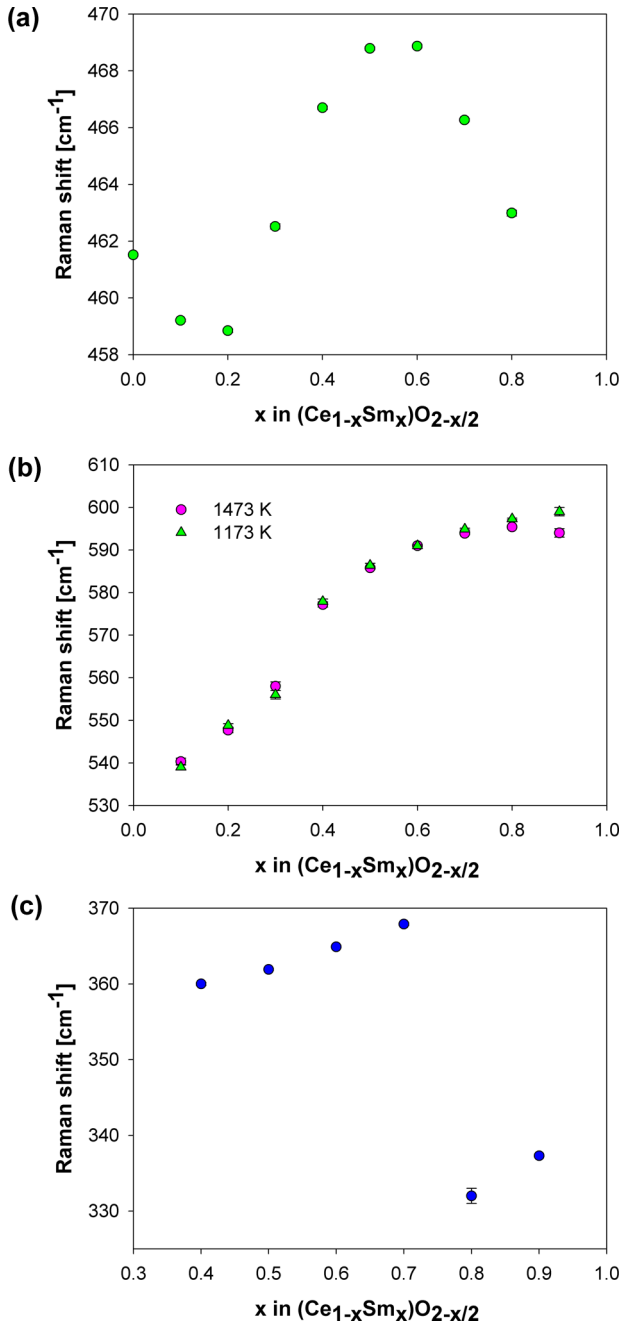

Figure 8. Peak frequencies of the Raman mode of Sm-doped ceria prepared at 1473 K at (a) ∼465 cm^{-1} (RE-O vibration with RE in eightfold coordination in the fluoritic structure), (b) ∼540 cm^{-1} (oxygen vacancies), and (c) ∼370 cm^{-1} (RE-O bond in C-RE_2O_3).

trends can be recognized, namely, a decreasing trend within the fluoritic stability region, a steep increase to $x \approx 0.5$, and a steep decrease to $x = 0.8$. Wave numbers of the signal associated with the oxygen vacancies at ∼540 cm^{-1} (Figure 8b) show an increase along the whole compositional range, and an irregularity between $x = 0.3$ and 0.4, that is, at the F/H boundary. In Sm-doped samples the increase becomes then less steep with increasing x until a saturation value of ∼595 cm^{-1} is reached for $x = 0.8$. Similarly, a saturation is observed also for the signal at ∼250 cm^{-1} in Sm-doped samples at $x \approx 0.6$, and an analogous, if even more scattered behavior, is observed in Gd-doped samples; the band at 190 cm^{-1}, on the contrary, shows a substantially constant value. Differently from the above-mentioned signals, the band at ∼370 cm^{-1}, originated by the presence of the C phase, shows a linear increase for $0.4 \leq x \leq 0.7$ and a sudden fall to values of ∼330 and 350 cm^{-1} for Sm- and Gd-doped samples, respectively (Figure 8c).

4. DISCUSSION

4.1. Stability Region of the Fluoritic Structure. As previously mentioned, patterns of samples with low x values (up to $x = 0.2$ and 0.3 in Gd- and Sm-doped samples, respectively) can be refined using the fluoritic structure as a model; thus, the introduction of small amounts of a trivalent rare earth into the CeO_2 structure takes place via randomly distributed Ce^{4+} substitution, with the absence of C-based superstructure peaks confirming the random character of the substitution. A linear trend of the cell parameter as a function of x within the fluoritic range is observed in Sm-containing samples; the existence of a solid solution in this compositional range can not be deduced by invoking Vegard's law because of two issues, namely, the absence of the value referred to hypothetic SmO_2, and the slight oxygen depletion that takes place within the fluoritic region, as observable in Figure 3. Vegard's law applies to systems where the total number of atoms does not change with composition; thus, in this case it is not expected to hold.[35] On the contrary, two main points allow to deduce that a solid solution forms: (a) the random substitution of Ce^{4+}, indirectly testified by the fact that C-based microdomains are not detectable by XRD; (b) the retention of the typical fluoritic value for the Ce/RE1 x position (0.25, see Figure 4), obtained by refining patterns using the hybrid model. This issue will be in more depth treated in the following paragraph, where the discussion will be extended to the whole compositional range.

Even if the fluoritic structure is retained, Raman results highlight the disturbing effect caused by the dopant introduction: the band at 465 cm^{-1} broadens, and signals related to the presence of oxygen vacancies appear even at the lowest doping amounts. Moreover, the presence of a broad band at ∼370 cm^{-1} already at $x = 0.2$ and 0.3 (for Gd- and Sm-doped ceria, respectively), evolving into the band typical of C RE_2O_3 at higher x values, points to the presence of several nanodomains with symmetry belonging to the $Ia\bar{3}$ space group; the presence of C-RE_2O_3 nanodomains, acting as oxygen vacancies traps, was also observed by transmission electron microscopy,[36,37] and it can explain the ionic conductivity reduction observed at x values higher than ∼0.1 and ∼0.2 for Gd- and Sm-doped samples,[2,38] respectively, that is, well within the fluoritic region.

The introduction of a trivalent ion in place of Ce^{4+} should in fact cause the formation of a certain amount of charge-balancing oxygen vacancies. Nevertheless, it can be observed in Figure 6 that in both systems the oxygen occupancy does not linearly decrease toward zero, since it remains higher than expected at each composition within the fluoritic region. This evidence can be attributed to the partial segregation of vacancies into the observed C-based RE_2O_3 nanodomains; the oxygen depletion deriving from segregated vacancies can not be observed by refining the oxygen occupancy, since the cited nanodomains are not appreciable by X-ray diffraction due to their very low amount.

DOI: 10.1021/acs.inorgchem.5b00395
Inorg. Chem. 2015, 54, 4126−4137

A closer analysis of the peak frequencies at ~465 cm^{-1} confirms that two factors contribute to the trend of the cited peak frequencies, namely, the bond length variation due to the Ce^{4+} substitution and the subsequent formation of oxygen vacancies. The latter phenomenon is generally expected to cause a lattice contraction and, consequently, a shift of Raman frequencies toward higher wave numbers. On the contrary, the substitution of Ce^{4+} by Sm^{3+}, as well as Gd^{3+}, causes a lattice expansion, being the CN8 ionic sizes of Ce^{4+}, Sm^{3+}, and Gd^{3+}, 0.97, 1.079, and 1.053, respectively;[6] a shift toward lower Raman frequencies is then expected. The separation of the two contributions can be performed by subtracting the size effect, as proposed by Mc Bride et al.,[27] who calculated the Raman shift due to the lattice volume variation:

$$\Delta\omega = -3\gamma\omega_0\Delta a/a_0 \quad (1)$$

where ω_0 is the Raman peak frequency of CeO_2, a_0 is the cell parameter of CeO_2, and γ is the Grüneisen constant, which depends on the CeO_2 bulk modulus and on the shift of Raman frequencies with hydrostatic pressure; according to the study performed by Sato and Tateyama,[39] the suggested value of γ is 1.24. The corrected values of Raman shifts both for Gd- and Sm-containing samples, calculated along the whole compositional range, are reported in Figure 9. Notice that, after the subtraction of the size effect, the trend of the peak frequencies within the fluoritic region is increasing, meaning that the formation of oxygen vacancies takes place. Moreover, by comparing the uncorrected data shown in Figure 8a with the corrected ones, it can be observed that the data of the two series almost coincide, revealing that the formation mechanism of oxygen vacancies does not differ between the two systems and that the differences observed in the uncorrected peak frequencies can be entirely ascribed to the size of the doping ion.

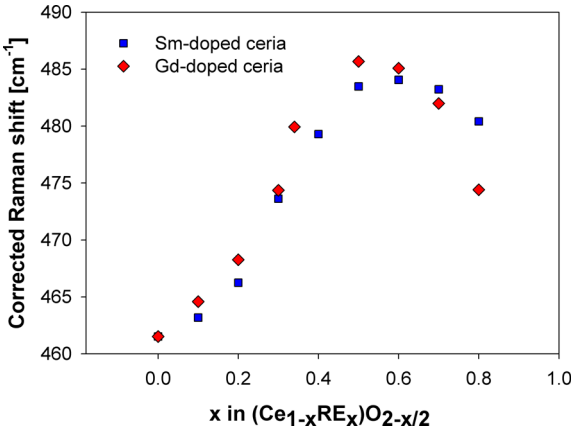

Figure 9. Corrected Raman shifts of the band at ~465 cm^{-1} by the lattice volume effect for Sm- and Gd-doped ceria as a function of RE content.

The effect of the vacancies formation must be taken into account also when considering the extent of the fluoritic stability region. The position of the cited boundary depends on the doping ion: according to the results of this study (for Sm- and Gd-doped samples) and literature data (for Nd- and La-doped samples),[18] a linear relation exists between the boundary position and the Ce^{4+}[CN8]/RE^{3+} [CN8] size difference: the closer the Ce^{4+} and the RE^{3+} sizes, the lower is the x value corresponding to the F/H boundary, that is, the narrower is the fluoritic stability region. If only the effect of the doping ion size is taken into account, this evidence appears to conflict with the expected behavior, which is an increase of the fluoritic stability range with increasing Ce^{4+}/RE^{3+} size similarity; nevertheless, the introduction of the trivalent ion is always accompanied by the formation of a certain oxygen vacancy amount, which induces a similar lattice contraction for each RE. The bigger the RE^{3+} ion is, the more efficiently it counterbalances the lattice shrinkage induced by oxygen vacancies.

4.2. Stability Region of the Hybrid Structure. The appearance of small superstructure peaks starting from a certain composition accounts for the splitting of the Ce/RE position into two different sites due to the strain induced in the fluoritic structure by the introduction of a foreign ion. The intensity of the superstructure peaks increases with increasing RE content; along with the absence of any peak splitting, this behavior justifies the adoption of a hybrid model for the refinement of patterns with x ranging between 0.3 and 0.9, as thoroughly discussed in previous papers.[13,14] The non-Vegard trend of cell parameters, observed also in the Ce−Sm system, confirms the nonexistence of any solid solution in this compositional range, and the absence of parameter saturation rules out the presence of a biphasic region, at least as commonly meant. By adopting the hybrid model, it is possible to follow the trend of some parameters that are particularly sensitive to the F → C transition, such as the O2 occupancy factor, as well as the Ce/RE1 x position. The most striking evidence coming from the refinements is the progressive shift of both parameters with increasing RE content toward the values typical of C RE_2O_3, indicating a gradual change from the fluoritic to the cubic C structure.

In more detail, the trend of the O2 occupancy factor as a function of RE content, shown in Figure 6, indicates for both systems the presence of two different behaviors, namely, a slight oxygen decrease within the fluoritic region, discussed in the previous paragraph, and a steeper decrease within the hybrid region. As a confirmation of the described F/H boundary position, the cited slope change is located at higher x in Sm-doped ceria than in Gd-doped ceria. The slope change can be taken as an indicator of the F/H boundary, because, differently from the fluoritic region, within the hybrid region the trend of the O2 occupancy factor can be satisfactorily interpolated by a regression line joining the occupancy factor at the boundary to a value of zero for both Gd- and Sm-doped ceria.

Data of Sm80_1473 and Sm90_1473, on the contrary, seem not to obey this trend, showing slightly higher occupancy values. Considering the XRD results, which account for the presence of a certain amount of B Sm_2O_3 in the aforementioned samples, an O2 occupancy factor higher than expected can be ascribed to the Sm subtraction due to the presence of the latter oxide, which moves the average composition of the mixed oxides toward a higher Ce content. According to the stability diagram of rare earth sesquioxides,[4] B Sm_2O_3 is expected to be stable at temperatures higher than ~1173 K; diffraction patterns collected on samples synthesized at this temperature show in fact a B Sm_2O_3 amount that is remarkably smaller than that in samples prepared at 1473 K (see Table 1). Correspondingly, the O2 occupancy factor of samples treated at 1173 K does not show any anomaly with respect to the regression line, confirming the described hypothesis. The presence of B Sm_2O_3 was detected also by μ-Raman spectroscopy: spectra of samples with x = 0.8 and 0.9 show in fact the presence of bands typical of this oxide at each

DOI: 10.1021/acs.inorgchem.5b00395
Inorg. Chem. 2015, 54, 4126−4137

temperature considered, even if the whole set of the typical Raman signals can be observed only in Sm90_1473, that is, in the sample where the highest amount of B Sm_2O_3 is also found by XRD. The detection of B Sm_2O_3 in samples where the presence of this oxide is not revealed by XRD is a sign of the high sensitivity of Raman spectroscopy and of its complementarity to XRD. Noteworthy is that a small amount of B Gd_2O_3, never revealed by XRD, can be observed also in Gd-doped ceria for x = 0.8 and 0.9; with reference to the stability diagram of rare earth sesquioxides,[4] the C/B structural boundary is in fact located in the close vicinity of 1473 K.

In addition to the behavior of the O2 occupancy factor, as previously mentioned, a further clear indication of a gradual change from the F to the C structure through the hybrid region can be found in the trend of the Ce/RE1 x position as a function of RE content, shown in Figure 4: within the hybrid region the x value moves in fact from the one typical of CeO_2 (0.25) to the one typical of C Gd_2O_3 (0.281) or C Sm_2O_3 (0.280).

The gradual character of the F → C transition is confirmed by the trend of the mean atomic volume as a function of composition, calculated by dividing the cell volume by the effective number of atoms per cell for each x value. This trend is reported in Figure 10: according to Zen's law,[40] the linear

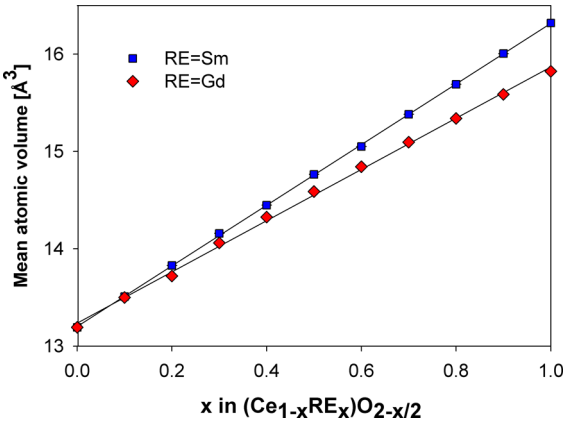

Figure 10. Trend of the mean atomic volume as a function of x for both series; regression lines are indicated too; error bars are hidden by data markers.

behavior observed indicates the existence of a solid solution along the whole compositional range; the higher slope value shown by Sm-doped ceria can be attributed to the larger size of Sm^{3+} with respect to Gd^{3+}.

The striking difference between the trend of the cell parameter and the mean atomic volume as a function of composition (see Figures 3 and 10, respectively) is a very interesting point, as the cited trends seem to conflict; it deserves an explanation, as it unveils a structural peculiarity of the studied systems, which will be further confirmed by Raman measurements. According to Vegard[41] and to Zen,[40] both trends should be able to reveal the existence of a solid solution within their linearity range. Nevertheless, as already discussed, Vegard's law is not obeyed even within the fluoritic stability range, that is, where RE^{3+} randomly substitutes Ce^{4+}. In this compositional range a linear trend is observed, not corresponding to Vegard's law, while at higher x values a parabolic behavior is detected. Zen's law, on the contrary, holds along the whole compositional range. The observed difference is attributable to the fact that, at variance with Vegard's law, Zen's law is defined by considering a normalized atomic volume. Thus, the linearity of the mean atomic volume indicates that solid solution forms in the fluoritic as well as in the hybrid range. While in the former region the solid solution is based on the fluoritic structure, in the so-called hybrid region it is based neither on the F nor on the C structure but on an intermediate one. In other words, when the experimentally observed oxygen depletion is taken into account, a hybrid F/C solid solution is observed from the F upper boundary up to C RE_2O_3, meaning that, with increasing x value, RE regularly accommodates within the intermediate structure. Differently from what happens in the fluoritic stability region, RE^{3+} does not randomly replace Ce^{4+}, but it tends to form aggregations where the Ce^{4+}/RE^{3+} ion occupies the two crystallographic sites typical of the C structure, and oxygen proportionally leaves the structure; that is, it forms C-based microdomains. Thus, the mean atomic volume trends show that, if observed from a global point of view, the RE^{3+} introduction causes the formation of a solid solution based on the F/C intermediate structure.

At this stage, it must be carefully considered that structural data derived from XRD diffraction provide an average crystallographic scenario that can only suggest hints about the local scale. Nevertheless, the gradual change of the F into the C structure observed within the hybrid region allows to hypothesize the presence of two so finely intergrown and interlaced phases, that they can not be distinguished, nor their exact composition can be detected, by this technique. A first indirect confirmation of this assumption can be found in the presence of a slope change of ∼0.5 in the trend of the Ce/RE1 x position, as well as in the RE1−RE1 bond distance, already mentioned in the Results Section. In both systems regression lines interpolating data at high ($0.5 \leq x \leq 1$) and medium (0.2 or $0.3 \leq x \leq 0.5$, for Gd- and Sm-based systems, respectively) RE content cross close to the value of 0.5, meaning that the mechanism leading to the slope change does not depend on the RE nature (see Figure 4). The same crossing points are reported also in Figure 5, showing that they mark the boundaries also in the trend of RE1−RE1 interatomic distances. Moreover, in Figure 4 the extrapolation of the regression line interpolating data at high RE content leads for both systems to the close vicinity of 0.25, that is, the value of CeO_2; the same evidence, even if not explicitly indicated in the figure for the sake of clarity, could be observed in the trend of the RE1−RE1 bond distances reported in Figure 5.

An interpretation of the described slope change can be found in a paper by Coduri et al.[15] that noted an analogous behavior in Y-doped ceria; by modeling the PDF's data, the authors deduced that at a local scale two phases are present, namely, a CeO_2- and a C-based one; moreover, they concluded that a CeO_2 matrix with C-based microdomains for $x < 0.5$, and a C-based matrix with embedded CeO_2-based microdomains for $x > 0.5$, are present. Our data related to Gd- and Sm-based systems support the evidence that the boundary position at ∼0.5, being independent from the RE nature, has a topological origin. On the basis of the described interpretation, 0.5 should be then the concentration at which percolation takes place; indeed, 0.5 is the percolation threshold of a randomly placed second phase in a square lattice,[42] which confirms the geometrical nature of the transition. Vertical lines are reported in Figure 4 also at lower RE amount: they are located at the crossing point between regression lines of data related to the F and the H region. Note

DOI: 10.1021/acs.inorgchem.5b00395
Inorg. Chem. 2015, 54, 4126−4137

that their position is different for different RE, thus confirming the chemical nature of the transition.

The presence of the two finely interspersed phases within the hybrid region can be directly observed by μ-Raman spectroscopy, which is able to give deep insight into the studied systems at the local scale for two main reasons: (a) the Raman bands of the F and C phase are well-distinguished; (b) the Raman technique is very sensitive to the oxygen displacement, so that even very small quantities of each of the two phases, as well as oxygen vacancies, can be detected. Moreover, even in ref 15, no hints are given about the Ce/RE ratio within the F and C phase, although the entrance of Gd atoms and oxygen vacancies into the F phase, as well as of Ce and O atoms into the C phase, are considered as highly probable. μ-Raman spectroscopy, on the contrary, can provide a qualitative indication of the composition changes occurring within the samples in the hybrid region, and suggest a possible explanation for the cell parameters trend.

The presence of Raman bands both at ~465 cm^{-1}, as well as at ~370 cm^{-1}, observable in Figure 7, allows to assert that F- and C-based microdomains are contemporarily present within the hybrid region. Moreover, basing on the intensity ratio of the two bands, it can be concluded that the C phase amount rises at the expense of the F phase with increasing x.

Regarding the composition of the two phases, the presence of a certain amount of oxygen vacancies in the F-based phase within the hybrid region is assured by the existence of the Raman bands at ~540, 250, and 190 cm^{-1}. To consider this point in more detail, the qualitative trend of the C and F phase composition can be followed by taking into account the shift of the main peak position of both phases with changing x. In particular, the peak position at ~465 cm^{-1}, corrected by subtraction of the doping ion size effect, is directly related to the oxygen vacancies variation within the fluoritic structure; the shift of the peak positions at ~370 cm^{-1}, on the contrary, is driven by the possible entrance into the Gd_2O_3 lattice of Ce^{4+} [CN6], which is characterized by a remarkably smaller radius (0.87 Å) than Sm^{3+} [CN6] (0.958 Å) or Gd^{3+} [CN6] (0.938 Å). The two curves reported in Figure 9, showing the corrected peak frequencies of the signal at ~465 cm^{-1} for both Sm- and Gd-based systems, show a substantial resemblance between the two systems, indicating that the mechanism of vacancy formation is essentially the same, irrespective of the RE identity. Notice that the peak values increase up to $x = 0.6$ and subsequently decrease, pointing to a lattice contraction related to the vacancies increase up to the maximum and to a lattice expansion due to the vacancy decrease for higher RE content. The discrepancy between the values at $x = 0.8$ is probably due to the presence of a significant amount of B Sm_2O_3 in Sm80_1473, which, as already described, shifts the average composition of the mixed oxides toward a lower Sm content. Correspondingly, the peak position of the band at ~370 cm^{-1} shows a slight increase in the Raman shift up to $x = 0.7$ and a sudden fall to lower values at higher x. The latter behavior can be reasonably ascribed to the transition of the C phase from $(Gd,Ce)_2O_3$ to substantially pure Gd_2O_3 with increasing x above 0.7. On the basis of this evidence, it can be concluded that the F-based microdomains continue incorporating Gd^{3+} ions and a corresponding amount of oxygen vacancies up to $x \approx 0.6$; beyond this value, Gd ions tend to leave the fluoritic structure, causing a decrease in the oxygen vacancies number. Within the whole hybrid region, the amount of F-based microdomains progressively decreases with increasing RE content; correspondingly, the number of C-based droplets rises, until the percolation threshold is reached, and the composition of both phases gets close to the one of CeO_2 and Gd_2O_3, respectively.

A further confirmation of the varying amount of vacancies in F-based microdomains can be found in the behavior of the peak frequencies of the Raman bands directly related to their presence, that is, the ones at ~540 and 250 cm^{-1}. Generally speaking, oxygen vacancies tend to distort the cell causing a lattice contraction in the closest coordination sphere; moreover, in RE^{3+}-doped ceria oxygen vacancies are commonly believed to interact with each other and to form clusters,[37,43,44] as the latter ensure an increasing dopant-vacancy binding energy with increasing cluster size. Raman bands involving vacancies are then expected to be characterized by higher wavenumber with increasing vacancies amount, as the cluster size increases too. An increase in the Raman shift is in fact observed with increasing x up to $x \approx 0.7$ for both Gd- and Sm-doped ceria, while at higher x values Raman shifts tend to a constant value. At the same time, the intensity of the band decreases with increasing x, meaning a progressive reduction in the number of F-based microdomains. The main difference between the Ce−Gd and Ce−Sm systems samples consists in a less steep increase in the peak wave numbers in Sm-doped samples at high x values: this evidence is reasonably attributable to the presence of a substantial B Sm_2O_3 amount that, as already discussed, shifts the global composition of the hybrid structure toward a higher Ce content. This hypothesis is confirmed by the trend of peak wave numbers of Sm-doped samples prepared at 1173 K, which shows higher values than samples prepared at 1473 K at high x (see Figure 8b). Similar conclusions can be drawn for the Raman band at ~250 cm^{-1}.

The non-Vegard behavior of the lattice parameter as a function of composition, observed for many RE^{3+}-doped ceria systems, and extensively studied in a vast number of papers,[43−45] is generally attributed to the interplay of dopant size and defects cluster formation; as shown in Figure 3, Sm- and Gd-doped ceria present such a behavior too. A discussion of the reasons of this trend are beyond the scope of the paper, but the qualitative investigation of the F- and C-based phase composition within the hybrid region provides elements to better understand the nature of the region itself. The formation of the two intimately interlaced phases, which can be treated neither as two separate phases nor as a single phase, takes place for the sake of energy minimization; thus, with changing RE^{3+} amount, both phases adapt their composition to mutually fit. The resulting lattice parameter is then a compromise between the dopant size (RE^{3+} in CeO_2 and Ce^{4+} in RE_2O_3) and the introduction of oxygen vacancies into the F-based structure.

The formulated scenario finds a confirmation by taking into account the stability of Sm_2O_3: although at 1473 K it is more stable in the monoclinic B form, it enters the CeO_2 structure forming microdomains characterized by the C structure, meaning that the driving factor of the mixed oxide formation is not the stability of the two single oxides, but the stabilization of the hybrid region, obtained by the adjustment of both phases composition.

5. CONCLUSIONS

Three main conclusions can be drawn by analyzing the structural data of $(Ce_{1-x}RE_x)O_{2-x/2}$ samples (RE ≡ Sm, Gd) deriving from X-ray powder diffraction and μ-Raman spectroscopy.

DOI: 10.1021/acs.inorgchem.5b00395
Inorg. Chem. 2015, 54, 4126−4137

- Two structural transitions can be observed as a function of RE^{3+} content: the first one, of chemical nature, located at different compositions depending on RE, and the second one, of geometrical nature, at $\sim x = 0.5$. The former marks the boundary between the fluorite-based solid solution and the hybrid region, while the latter is positioned at the percolation threshold, that is, at the composition where the F-based matrix with embedded C-based microdomains changes into a C-based matrix with embedded F-based microdomains. The percolation threshold position depends on the lattice geometry, and for a square lattice it is expected at the equimolar composition.
- The composition of the F- and the C-based interspersed phases stable in the hybrid region changes with changing RE^{3+} content to allow the two structures to fit each other and thus to reach a condition of minimum energy. In particular, the F and the C phases enrich in RE^{3+} and Ce^{4+}, respectively, up to $x \approx 0.6$, while at higher RE content their composition tends to approach the one of CeO_2 and RE_2O_3, respectively.
- A certain amount of B Sm_2O_3 is recognizable by XRD in samples Sm80_1473, Sm90_1473, and Sm90_1173. This evidence is due to the higher stability of the monoclinic structure of Sm_2O_3 with respect to the cubic one at the cited temperatures. As a consequence, the global composition of the mixed oxide is shifted toward a higher Ce content than expected from the nominal composition. Very small amounts of the monoclinic phase could be detected by μ-Raman spectroscopy also in Gd-rich Gd–Ce mixed oxides, thanks to the very high sensitivity of this technique.

■ ASSOCIATED CONTENT

Supporting Information

Crystallographic structures illustrated in CIF files, Rietveld plots, starting Rietveld models, table containing thermal parameters and agreement factors, results of Rietveld refinements on B Sm_2O_3, and Raman peak frequencies. This material is available free of charge via the Internet at http://pubs.acs.org.

■ AUTHOR INFORMATION

Corresponding Author

*E-mail: artini@chimica.unige.it. (C.A.)

Author Contributions

The manuscript was written through contributions of all authors. All authors have given approval to the final version of the manuscript.

Notes

The authors declare no competing financial interest.

■ ACKNOWLEDGMENTS

The Elettra Synchrotron Radiation Facility is kindly acknowledged for the provision of beam time. The authors wish to thank Dr. A. Lausi for assistance in performing measurements at the MCX beamline and Prof. F. Merlo for the helpful discussions.

■ REFERENCES

(1) Skinner, S. J.; Kilner, J. A. *Mater. Today* **2003**, *6*, 30–37.
(2) Steele, B. C. H. *Solid State Ionics* **2000**, *129*, 95–110.
(3) Tianshu, Z.; Hing, P.; Huang, H.; Kilner, J. *Solid State Ionics* **2002**, *148*, 567–573.
(4) Eyring, L. In *Handbook on the Physics and Chemistry of Rare Earths;* Gschneidner, K. A., Jr., Eyring, L., Eds.; Elsevier: Amsterdam, **1979**, *3*, 337–399.
(5) Varez, A.; Garcia Gonzalez, E.; Sanz, J. *J. Mater. Chem.* **2006**, *16*, 4249–4256.
(6) Shannon, R. D. *Acta Crystallogr.* **1976**, *A32*, 751–767.
(7) Ubaldini, A.; Artini, C.; Costa, G. A.; Carnasciali, M. M.; Masini, R. *J. Therm. Anal Calorim.* **2006**, *84*, 207–211.
(8) Eyring, L. In *Handbook on the Physics and Chemistry of Rare Earths;* Gschneidner, K. A., Jr., Eyring, L., Eds.; Elsevier: Amsterdam, **1979**, *3*, 401–524.
(9) Zhang, T. S.; Ma, J.; Kong, L. B.; Chan, S. H.; Kilner, J. A. *Solid State Ionics* **2004**, *170*, 209–217.
(10) Ikuma, Y.; Takao, K.; Kamiya, M.; Shimada, E. *Mater. Sci. Eng.* **2003**, *B99*, 48–51.
(11) Grover, V.; Tyagi, A. K. *Mater. Res. Bull.* **2004**, *39*, 859–866.
(12) Peng, C.; Zhang, Z. *Ceram. Int.* **2007**, *33*, 1133–1136.
(13) Artini, C.; Costa, G. A.; Pani, M.; Lausi, A.; Plaisier, J. *J. Solid State Chem.* **2012**, *190*, 24–28.
(14) Artini, C.; Pani, M.; Lausi, A.; Masini, R.; Costa, G. A. *Inorg. Chem.* **2014**, *53*, 10140–9.
(15) Coduri, M.; Scavini, M.; Allieta, M.; Brunelli, M.; Ferrero, C. *Chem. Mater.* **2013**, *25*, 4278–4289.
(16) Coduri, M.; Scavini, M.; Brunelli, M.; Masala, P. *Phys. Chem. Chem. Phys.* **2013**, *15*, 8495–8505.
(17) Scavini, M.; Coduri, M.; Allieta, M.; Brunelli, M.; Ferrero, C. *Chem. Mater.* **2012**, *24*, 1338–1345.
(18) Horlait, D.; Claparède, L.; Clavier, N.; Szencnekt, S.; Dacheux, N.; Ravaux, J.; Podor, R. *Inorg. Chem.* **2011**, *50*, 7150–7161.
(19) Acharya, S. A.; Gaikwad, V. M.; D'Souza, S. W.; Barman, S. R. *Solid State Ionics* **2014**, *260*, 21–29.
(20) Grover, V.; Banerji, A.; Sengupta, P.; Tyagi, A. K. *J. Solid State Chem.* **2008**, *181*, 1930–1935.
(21) Costa, G. A.; Artini, C.; Ubaldini, A.; Carnasciali, M. M.; Mele, P.; Masini, R. *J. Therm. Anal. Calorim.* **2008**, *92*, 101–104.
(22) Ubaldini, A.; Artini, C.; Costa, G. A.; Carnasciali, M. M.; Masini, R. *J. Therm. Anal. Calorim.* **2008**, *91*, 797–803.
(23) Rodriguez-Carvajal, J. *Phys. B* **1993**, *192*, 55–69.
(24) Villars, P.; Cenzual, K. *Pearson's Crystal Data-Crystal Structures Database for Inorganic Compounds;* ASN International: Materials Park, OH, 2014.
(25) Wu, B.; Zinkevich, M. V.; Aldinger, F.; Wen, D.; Chen, L. *J. Solid State Chem.* **2007**, *180*, 3280–3287.
(26) Weber, W. H.; Hass, K. C.; Mc Bride, J. R. *Phys. Rev. B* **1993**, *48*, 178–185.
(27) Mc Bride, J. R.; Hass, K. C.; Poindexter, B. D.; Weber, W. H. *J. Appl. Phys.* **1994**, *76*, 2435–2441.
(28) Nakajima, A.; Yoshihara, A.; Ishigame, M. *Phys. Rev. B* **1994**, *50*, 13297–13307.
(29) Esther Jeyanthi, C.; Siddheswaran, R.; Kumar, P.; Siva Shankar, V.; Rajarajan, K. *Ceram. Int.* **2014**, *40*, 8599–8605.
(30) Zhou, Y.; Rahman, M. N. *J. Mater. Res.* **1993**, *8*, 1680–1686.
(31) Aškrabić, S.; Dohčević-Mitrović, Z. D.; Radović, M.; Šćepanović, M.; Popović, Z. V. *J. Raman Spectrosc.* **2009**, *40*, 650–655.
(32) Ubaldini, A.; Carnasciali, M. M. *J. Alloys Compd.* **2008**, *454*, 374–378.
(33) Mandal, B. P.; Roy, M.; Grover, V.; Tyagi, A. K. *J. Appl. Phys.* **2008**, *103*, 033507/1–7.
(34) Mandal, B. P.; Grover, V.; Roy, M.; Tyagi, A. K. *J. Am. Ceram. Soc.* **2007**, *90*, 2961–2965.
(35) A test aimed to verify this hypothesis was done based on geometrical considerations: a calculated value of cell parameters was obtained from interatomic distances, with the latter deriving from the sum of Sm^{3+} [C.N.:8] and O^{2-} sizes; the discrepancy between the so-calculated and the experimental values lies within 1% at $x = 0.2$ and increases to 2.5% at $x = 1$; similar results can be obtained if the Ce–Gd system is considered. The increasing difference between calculated

DOI: 10.1021/acs.inorgchem.5b00395
Inorg. Chem. 2015, 54, 4126–4137

and experimental value of the cell parameter with increasing x can be ascribed to the oxygen depletion; nevertheless, this result does not imply that a solid solution does not form in this compositional range, but it does imply that Vegard's law is not suitable to describe such a system.
(36) Ye, F.; Mori, T.; Ou, D. R.; Zou, J.; Drennan, J. *Solid State Ionics* **2009**, *180*, 1414−1420.
(37) Ou, D. R.; Mori, T.; Ye, F.; Zou, J.; Auchterlonie, G.; Drennan, J. *Phys. Rev. B* **2008**, *77*, 0240108 1−8.
(38) Peng, C.; Wang, Y.; Jiang, K.; Bin, B. Q.; Liang, H. W.; Feng, J.; Meng, J. *J. Alloys Compd.* **2003**, *349*, 273−278.
(39) Sato, T.; Tateyama, S. *Phys. Rev. B* **1982**, *26*, 2257−2260.
(40) Zen, E. *Am. Mineral.* **1956**, *41*, 523−524.
(41) Vegard, L.; Dale, H. *Z. Kristallogr.* **1928**, *67*, 148−162.
(42) Isichenko, M. B. *Rev. Mod. Phys.* **1992**, *64*, 961−1043.
(43) Wang, B.; Lewis, R. J.; Cormack, A. N. *Acta Mater.* **2011**, *59*, 2035−2045.
(44) Minervini, L.; Zacate, M. O.; Grimes, R. W. *Solid State Ionics* **1999**, *116*, 339−349.
(45) Nakamura, A. *Solid State Ionics* **2010**, *181*, 1631−1653.

DOI: 10.1021/acs.inorgchem.5b00395
Inorg. Chem. 2015, 54, 4126−4137